Simultaneous measurement of nanoscale electric and magnetic optical fields

B. le Feber[1]*, N. Rotenberg[1], D. M. Beggs[1,2] and L. Kuipers[1]*

Control of light–matter interactions at the nanoscale has advanced fields such as quantum optics[1], photovoltaics[2] and telecommunications[3]. These advances are driven by an improved understanding of the nanoscale behaviour of light, enabled by direct observations of the local electric fields near photonic nanostructures[4–6]. With the advent of metamaterials that respond to the magnetic component of light[7,8], schemes have been developed to measure the nanoscale magnetic field[9–12]. However, these structures interact not only with the magnetic field, but also with the electric field of light. Here, we demonstrate the essential simultaneous detection of both electric and magnetic fields with subwavelength resolution. By explaining our measurements through reciprocal considerations, we create a route towards designing probes sensitive to specific desired combinations of electric and magnetic field components. Simultaneous access to nanoscale electric and magnetic fields will pave the way for new designs of optical nanostructures and metamaterials.

For over 20 years, near-field scanning optical microscopy (NSOM) has improved our understanding of the flow and behaviour of light in and around nanophotonic structures[13]. Although the interaction of light with nanoscopic structures typically populates all six components of the electromagnetic near-field, maps of two components of the local optical electric fields have been sufficient to clarify and uncover exciting phenomena such as control of surface plasmon polaritons[4,14], field enhancements near nano-antennas[5,15] and polarization singularities[16]. The recent advent of metamaterials has sparked research in the nanophotonic structures that couple strongly not only to the electric field but also to the magnetic field of light[17], with the potential to cloak objects[18], show giant nonlinear optical activity[19] or exhibit a negative refractive index[20]. Consequently, a measurement of the complete nanoscale electromagnetic field vector is a powerful way to drive advances in the field of metamaterials, and to elucidate the interplay between optical behaviour and geometry that underpins these phenomena.

An ideal measurement would allow for the simultaneous mapping of both electric and magnetic fields in and around nanophotonic structures. In principle, using Maxwell's equations, it is possible to derive the full electromagnetic field vector if three of its components are known (in both amplitude and phase) in a three-dimensional space with sufficient accuracy for the derivatives to be taken. However, although such an approach is at the heart of many numerical simulations, the experimental equivalent has not been demonstrated at the nanoscale where all components are typically present. That is, to date, no more than two field components have been measured simultaneously[5,11,15,16]. Consequently, Maxwell's equations can only be exploited on certain planes of symmetry[11] and not in general.

Here, we demonstrate a direct mapping of all in-plane electromagnetic near-fields with a conventional, symmetric aperture probe (Fig. 1a), which has traditionally been assumed to detect either the electric fields[16] or *only* the in-plane magnetic field[9,21]. We show that the ratio of the efficiencies with which the magnetic field and the electric field are collected is between 0.3 and 2.5, and we also explain and predict this relative sensitivity through reciprocal considerations[22,23].

We image the evanescent fields above a photonic-crystal waveguide (PhCW) using a homebuilt, polarization-sensitive NSOM. A PhCW is an ideal structure for studying near-field detection, as the electromagnetic field distribution of its modes is well understood, while not being trivial[24]. Our PhCW is a 220 nm thin silicon slab perforated by a hexagonal lattice of holes with radii of 120 nm. One row of missing holes acts as a waveguide for the 1,570 nm transverse electric (TE) polarized light. A two-dimensional field map is created by raster scanning an aperture probe in the x–y plane above the nanophotonic structure (Fig. 1b). We ensure that all light resulting from an x-oriented electric field above the PhCW, E_x, is collected by detector L_x, and likewise E_y is detected by L_y. Any light that might arise from an x-oriented magnetic field, H_x, would be detected by L_y, and H_y would be picked up by L_x.

The three-dimensional structure of the PhCW allows us to use measurements at increasing heights h above the crystal to differentiate between $\mathbf{E}_{\|}$ and $\mathbf{H}_{\|}$. In the x–y plane of symmetry, inside the silicon membrane, only TE components (E_x, E_y, H_z) of the electromagnetic field are non-zero. However, away from this symmetry plane, all six components can be found[24,25]. Furthermore, these profiles have an intricate subwavelength structure, as reflected by our calculations of the fields 20 nm above the waveguide (Fig. 1c–e), which assists in the identification of the different field components. The corresponding measurements for L_x and L_y (Fig. 1f,g) are in excellent agreement with the calculated, in-plane components of the mode (Fig. 1c,d). Note that we show half the field profile of each mode, because the symmetry of the waveguide enforces mirror symmetry in x of the field amplitude of the mode. This data not only shows the good polarization separation of our system, but it also highlights that the fields mapped at the surface of the PhCW could equally be E_x and E_y (ref. 16) or H_y and H_x.

However, as h increases, not only do the relative amplitudes of the electric and magnetic fields change, but so do their spatial profiles. This divergence of the different field profiles occurs because a given mode is composed of a superposition of many Bloch harmonics, each of which decays differently in z (ref. 26). Furthermore, because $\mathbf{E}$ and $\mathbf{H}$ are related through their spatial derivatives, each field profile shows a different height dependence. This is reflected in Fig. 2a,b, which depicts the calculated amplitudes of E_x (and H_y) and E_y (and H_x), respectively, for different values of h. Notably, for $h > 250$ nm, E_x has minima along the centre of the waveguide, whereas H_y has maxima (arrows, Fig. 2a). In addition, at these large heights, the amplitude at the side of the waveguide of H_x is clearly larger than that of E_y (arrows, Fig. 2b).

[1]FOM Institute AMOLF, Science Park 104, Amsterdam 1098 XG, The Netherlands, [2]HH Wills Physics Laboratory, Tyndall Avenue, Bristol BS8 1TL, UK.
*e-mail: lefeber@amolf.nl; kuipers@amolf.nl

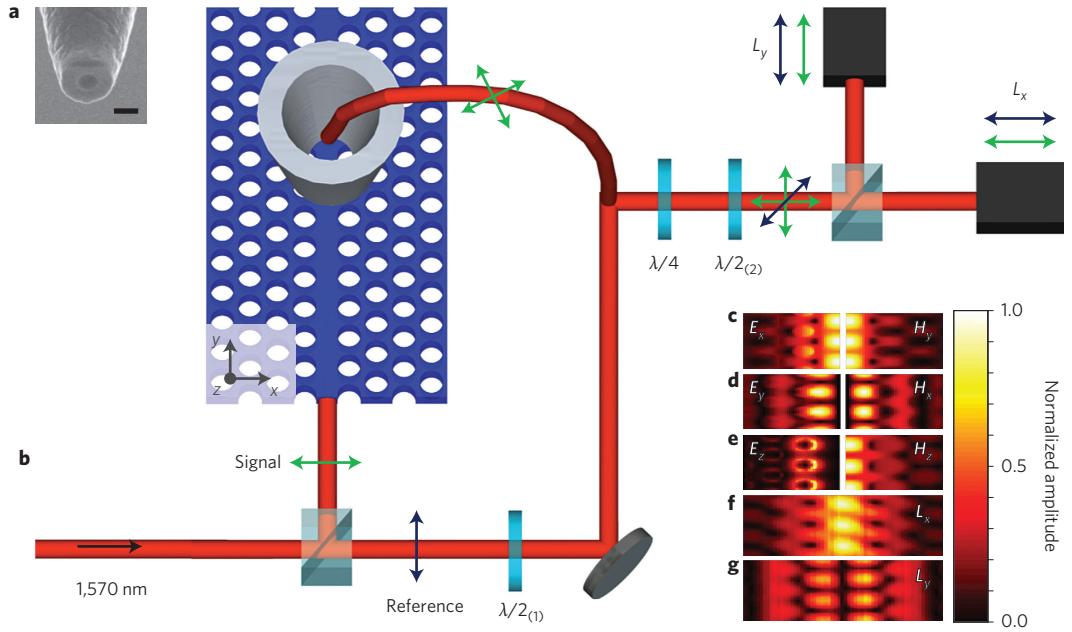

Figure 1 | NSOM measurements of a PhCW. a, SEM image of the apex of a typical near-field probe. This consists of a 218-nm-wide glass core coated with 200-nm-thick aluminium cladding. Scale bar, 500 nm. **b**, Schematic of the NSOM set-up. L_x and L_y represent two photodetectors coupled to lock-in detectors. The dark blue and green arrows indicate the polarization of the reference and signal branches, respectively. The two cubes are polarizing beamsplitter cubes, and $\lambda/2_{(2)}$ and $\lambda/4$ are used to orient the polarization of the light such that light from E_x ends up on L_x and E_y on L_y, and $\lambda/2_{(1)}$ is used to split the reference branch equally over the detectors. **c**–**e**, Calculations of the transverse fields. Left: electric field along *x*, *y* and *z*, respectively. Right: magnetic fields along *y*, *x* and *z*, respectively. **f**,**g**, Measurements taken 20 nm above the sample on L_x (**f**) and L_y (**g**). Panels **c**–**g** all show amplitudes, and are scaled to their respective maxima. All panels are 3 × 3 unit cells and for clarity are stretched in the *x*-direction.

The left panels of Fig. 2c,d depict how the measured field patterns evolve with height. Surprisingly, we observe that, as the height increases, the measurements correspond to neither the calculated $\mathbf{E}_{\|}$ nor $\mathbf{H}_{\|}$ profiles. For L_x we observe a minimum along the centre of the waveguide that is reminiscent of E_x (arrow, Fig. 2c). In contrast, for L_y we measure the enhanced side lobes expected for H_x. Yet, the response at the centre of the waveguide appears suppressed (arrow, Fig. 2d). These observations suggest that we measure a superposition of $\mathbf{E}_{\|}$ and $\mathbf{H}_{\|}$. By fitting the amplitude of the superposition of the two calculated complex fields to our data,

$$L_x(\mathbf{r}) = \alpha_x E_x(\mathbf{r}) + \beta_x H_y(\mathbf{r}) \tag{1a}$$

and

$$L_y(\mathbf{r}) = \alpha_y E_y(\mathbf{r}) + \beta_y H_x(\mathbf{r}) \tag{1b}$$

where $\mathbf{r} = (x, y)$ represents the position at which we measure the fields, we find $\alpha_{x,y}$ and $\beta_{x,y}$ that are complex scalars that quantify the sensitivity of our system to the electric and magnetic in-plane fields, respectively. We chose our unit system such that the electric and magnetic fields are in the same units, so if $|\alpha| = |\beta|$, the probe is equally sensitive to the electric and magnetic fields.

The right panels of Fig. 2c,d depict fits to measurements obtained at different heights for each detector. For all heights we find that the fit of the in-plane fields excellently reproduces all the features in the data. Importantly, we use only the four complex fit parameters, $\alpha_{x,y}$ and $\beta_{x,y}$, to fit all nine heights ranging from 20 nm to 380 nm simultaneously. For this particular probe, with a 218 nm diameter, we find that $|\beta_x|/|\alpha_x| = 0.5(2)$ and that $|\beta_y|/|\alpha_y| = 0.9(3)$. These values indicate that we detect roughly equal amounts of the electric and magnetic near-fields. In stark contrast to previous work that assumed that either the electric[16] or the magnetic[9,27] fields are detected, we show that we can simultaneously detect nanoscale electric and magnetic fields.

Our results are supported by recent work[28,29] that not only shows that single subwavelength holes in a metal have both a magnetic and an electric polarizability of comparable magnitude, but also highlights the hole-size dependence of the ratio of these polarizabilities. Therefore, we investigate the sensitivity to $\mathbf{E}_{\|}$ and $\mathbf{H}_{\|}$ of probes with different diameters. Figure 3a depicts a plot of the relative sensitivity ($|\beta|/|\alpha|$) for the two detectors L_x and L_y. This figure shows that probes of all diameters detect both $\mathbf{E}_{\|}$ and $\mathbf{H}_{\|}$. Owing to the cylindrical symmetry of our probe, we expect the relative sensitivities of L_x and L_y to overlap, which they do to within experimental error (see Methods). We attribute the experimental error to a contribution of the finite width of the probe, fabrication imperfections, tilt in probe orientation and/or height drift. For example, a slightly elliptical rather than circular aperture could break the symmetry between L_x and L_y.

To expand our understanding, we compare our measurements to the expected signals, calculated using the reciprocity theorem for electromagnetism, which effectively states that the detected signal from a source will be the same when source and detector are exchanged. This theorem enables us to relate the fields picked up by our probe to the fields transmitted through it when a (dipole) source is placed at the position of the detector[22]. Mathematically, the expected signal (L_i, where $i = x, y$) can then be expressed as (see Supplementary Information)

$$L_i(\mathbf{r}) \propto \int_S \left(\mathbf{E}_{\text{phc}} \times \mathbf{H}^i_{\text{rec}}(\mathbf{r}) - \mathbf{E}^i_{\text{rec}}(\mathbf{r}) \times \mathbf{H}_{\text{phc}} \right) \cdot \mathrm{d}\mathbf{S} \tag{2}$$

where we take $\mathbf{S}$ to be in the x–y plane ($\mathrm{d}\mathbf{S} = \mathbf{z}\mathrm{d}S$) and we neglect any back-action from the probe. Here, $\mathbf{r}$ is the position of the tip above the crystal, $\mathbf{E}_{\text{phc}}$ indicates the calculated E-fields above the waveguide, and $\mathbf{E}_{\text{rec}}$ indicates the fields under the tip resulting from an x- or y-oriented electric dipole placed at the detector position. We immediately recognize that the reciprocal magnetic field determines the sensitivity of the probe to the electric field ($\alpha \propto \int_S \mathbf{E}_{\text{phc}} \times \mathbf{H}^i_{\text{rec}} \cdot \mathrm{d}\mathbf{S}$) and vice

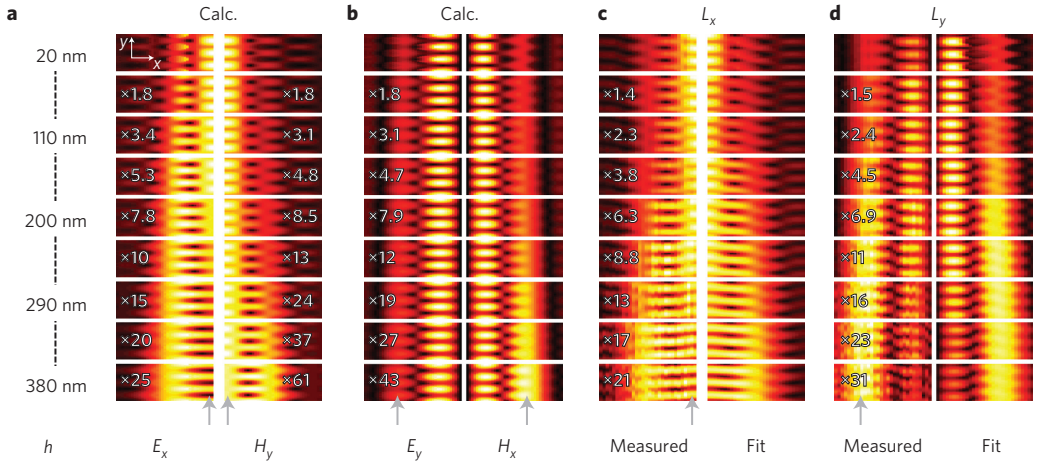

Figure 2 | Slices in the *x*-*y* plane at height *h* above the surface. a,**b**, Calculations of the evanescent field above the crystal. In **a**, the left column shows E_x left of the symmetry plane and the right column shows H_y right of the symmetry plane. In **b**, the left and right columns show in-plane field profiles of E_y and H_x, respectively. **c**, Left: fields measured on L_x. Right: fitted calculations. **d**, Left: fields measured on L_y. Right: fitted calculations. All plots show amplitudes of the calculated or measured signals. The colour in all plots is scaled to the maximum; scaling relative to the ground plane is indicate by the multiplication factors. All panels are 3 × 3 unit cells, and for clarity they are stretched in the *x*-direction. The axis orientation is show in the top E_x panel.

versa ($\beta \propto \int_S \mathbf{E}_{\mathrm{phc}} \times \mathbf{H}^i_{\mathrm{rec}} \cdot \mathrm{d}\mathbf{S}$), and that only the in-plane components of $\mathbf{E}_{\mathrm{phc}}$ and $\mathbf{H}_{\mathrm{phc}}$ contribute to the detected signal.

We can draw another subtle, yet important conclusion from these expressions. The reciprocity theorem tells us that our sensitivity is determined by the fields associated with both the sample and the probe. That is, what is detected depends not only on the probe used in the measurement, but also on the fields that are being measured. The reciprocal fields associated with the probe ($\mathbf{E}_{\mathrm{rec}}$, $\mathbf{H}_{\mathrm{rec}}$) have nanoscopic structure (see Supplementary Section 'Reciprocity'), as do the near-fields of nanophotonic structures such as our photonic crystal ($\mathbf{E}_{\mathrm{phc}}$, $\mathbf{H}_{\mathrm{phc}}$, Fig. 2). Furthermore, as we know from the reciprocity theorem, what we detect is a product of both fields. In essence, the $\mathbf{E}_{\mathrm{rec}}$ and $\mathbf{H}_{\mathrm{rec}}$ act like a spatial filter and, consequently, the sensitivity of the probe is dependent on which parts of $\mathbf{E}_{\mathrm{phc}}$ and $\mathbf{H}_{\mathrm{phc}}$ are allowed through.

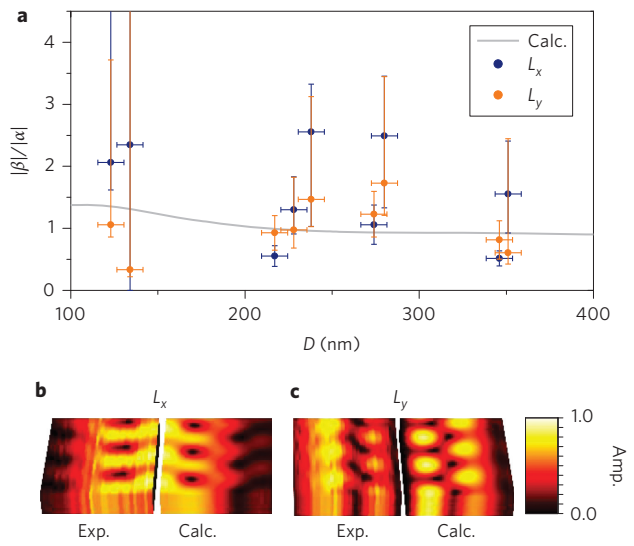

Figure 3 | Probe size dependent sensitivities. a, For probe diameters *D* from 120 nm to 350 nm we show $|\beta|/|\alpha|$ for both detectors, together with the calculated $|\beta|/|\alpha|$. Grey line: calculated $|\beta|/|\alpha|$ ratio. **b**,**c**, Right panels: *ab initio* calculations. Left panels: measured fields 300 nm above the PhCW on L_x and L_y, respectively. All panels are 3 × 3 unit cells and show signal amplitudes.

Figure 3b,c compares the calculated, predicted signals and the measured signals 300 nm above the PhCW. We find that the fields calculated with this *ab initio* approach closely match the measured field patterns. To extract a theoretical value for $|\beta|/|\alpha|$ (grey line, Fig. 3a), we compute the ratio of the signal from the electric field to the signal from the magnetic field. We average over a unit cell, all heights and over the two detectors (see Supplementary Section 'Relative sensitivity to **E** and **H**'). The excellent agreement of these calculations with the measured ratio (close to one) confirms that aperture probes of all radii are sensitive to both $\mathbf{E}_{\parallel}$ and $\mathbf{H}_{\parallel}$. Furthermore, the reciprocal framework not only explains our data, but can also be used for future probe designs that selectively detect certain electromagnetic field components.

In conclusion, we have demonstrated the simultaneous detection of the electric and magnetic optical fields at the nanoscale. We show that a symmetric aperture probe measures all four in-plane components of the electromagnetic field at once. The superposition of electric and magnetic fields that we detect can be extended to a full vectorial map using Maxwell's relations in combination with additional constraints; these can be provided by the symmetry properties of the sample or, alternatively, by measurements with different probes. These auxiliary measurements could be performed with a split-ring probe that is known to measure H_z (ref. 30), or a scattering-type NSOM that detects E_z (ref. 15). Our current work, coupled with the aforementioned techniques, and in conjunction with the use of reciprocity to inspire novel probe designs, provides a route to a full mapping of the electromagnetic fields at the nanoscale. This will open up new avenues towards the understanding and smart design of photonic nanostructures, such as split-ring resonators, that manipulate electric and magnetic fields. Concurrently, this work paves the way for studies of fundamental processes such as, for example, a molecule undergoing a magnetic dipole transition[10].

Methods

Three-dimensional near-field scanning microscopy above a PhCW. To avoid introducing artefacts into the measurements as a result of probe imperfections, we imaged each probe with a scanning electron microscope (SEM) both before and after each measurement. Each probe appeared circular to within the image resolution, as shown in Fig. 1a. We also ensured, in our measurements, that our probe was optimally normal to the PhCW. When measuring above this PhCW, we detected both a forward and a backward propagating Bloch mode due to a reflection from the end facet of the PhCW. In this Letter, we show only the forward-travelling waves, which we obtained by Fourier filtering out the backward-travelling Bloch wave[16]. We distinguished between the forward- and backward-propagating modes with the use of the phase information of the light, which we obtained with a heterodyne detection scheme (Fig. 1), by shifting

the reference branch frequency by 40 kHz with two acousto-optic modulators (not shown). The reference and signal branch were joined in a fibre splitter, which guided the light to two lock-in detectors, as described in the main text. We used $\lambda/2_{(1)}$ to balance the intensity of the reference branch over the detectors, and $\lambda/2_{(2)}$ and $\lambda/4$ (sketched in Fig. 1a) to compensate for the birefringence of the probe fibre, which would cause mixing of the signals between L_x and L_y. We exploited the symmetry of the photonic-crystal fields (Fig. 1c,d) to ensure that L_x and L_y detected only the symmetric and asymmetric signals, respectively. In essence, we ensured that the maximum on L_x overlapped with the zero on L_y at the centre of the waveguide, and maximized the ratio between them. Typically, we found ratios in excess of 50:1.

We used a force feedback loop to keep the probe at the sample when scanning the surface of the photonic crystal. However, if $h > 20$ nm, we could no longer use the force feedback, so we therefore switched to a quadrant-cell-based height feedback loop. In this mode of operation we compared the position of the probe as measured with the quadrant cell when it was scanning the surface of the sample. This meant there was now no longer direct feedback for the probe–sample distance, so these measurements could be affected by drift between the probe and the sample. We corrected for this possible drift by matching the decay of the field above the photonic crystal to the decay of the MIT photonic bands (MPB)[25] calculations, by scaling the height at which the data were computed. We found less than 10 nm h^{-1} drift for the measurements presented in this work.

Calculation of the waveguide eigenmodes and dispersion. The PhCW was a W1 waveguide, which was missing a row of holes in a 220-nm-thin silicon membrane perforated with a hexagonal pattern of holes (Fig. 1c). Light was confined in the plane of the waveguide by the photonic bandgap of the surrounding holes, and was confined to the silicon slab by total internal reflection. Our waveguide had a hole separation of $a = 420$ nm and a hole radius of $r = 120$ nm $= 0.29a$.

The waveguide eigenmodes $\mathbf{E}_k(\mathbf{r})$ and $\mathbf{H}_k(\mathbf{r})$ and eigenfrequencies $\omega(k)$ were calculated with the freely available MPB[25], which determines the Bloch eigenmodes of the structure using a plane-wave basis set and periodic boundary conditions. We used a supercell of dimensions $a \times 11a\sqrt{3} \times 10h$, where a is the lattice constant of the photonic crystal and h is the thickness of the silicon slab. This supercell was sufficiently large to avoid interactions between neighbouring supercells and the calculations used a grid size of $a/16$, which ensured convergence of the eigenvalues to better than 0.1%. The refractive index of silicon used was modelled to be 3.48, which is suitable for wavelengths around 1,570 nm.

The dispersion of PhCW modes is well known. The waveguide mode forms a continuous band within the photonic bandgap of the lattice. This band is interesting, as it contains a wide variety of near-field profiles, which we can probe simply by adjusting the frequency of the incident light. Here, we selected the waveguide mode at a wavelength of 1,570 nm.

Fabricating the waveguides. The fabrication of the PhCW began with a silicon-on-insulator wafer (SOITEC, 220 nm silicon layer/2 μm SiO_2 buffer). Electron-beam lithography was used to generate the required patterns in a resist (350 nm of ZEP 520-A, Zeon Chemicals), which were transferred directly into the silicon layer of the wafer using reactive ion etching with an SF_6/CHF_3 gas mix. After removing the remaining resist, the SiO_2 buffer was selectively removed from beneath the PhCW region using a dilute HF solution, thus forming a silicon membrane in the area of the PhCW. The access waveguides feeding the PhCW were protected from the HF by a layer of S1818 (Shipley), which was spun on before the HF step.

Error analysis. We identified the height drift (maximally 10% of height), the uncertainty of the x–y position (30 nm in each direction) and our exact location on the calculated dispersion relation of the PhCW as sources of error in our estimation of $|\beta|/|\alpha|$, for each probe. We then swept through this four-parameter space, and for each permutation used the fitting procedure outlined in the text (equation (1)) to find a value for α_i and β_i. In this manner, we obtained a spread of $|\beta|/|\alpha|$ values for these ratios (Fig. 3a; standard deviation indicated as error bars). Possible errors in our estimation of the probe diameter—tilt in probe orientation and fabrication imperfections—effectively change the diameter of the probe. This uncertainty is reflected in the error bars for D (Fig. 3a).

Received 10 July 2013; accepted 31 October 2013;
published online 15 December 2013

References

1. O'Brien, J. L., Furusawa, A. & Vučković, J. Photonic quantum technologies. *Nature Photon.* **3,** 687–695 (2009).
2. Atwater, H. A. & Polman, A. Plasmonics for improved photovoltaic devices. *Nature Mater.* **9,** 205–213 (2010).
3. Liu, X., Osgood, R. M., Vlasov, Y. A. & Green, W. M. J. Mid-infrared optical parametric amplifier using silicon nanophotonic waveguides. *Nature Photon.* **4,** 557–560 (2010).
4. López-Tejeira, F. *et al.* Efficient unidirectional nanoslit couplers for surface plasmons. *Nature Phys.* **3,** 324–328 (2007).
5. Dorfmüller, J. *et al.* Near-field dynamics of optical Yagi-Uda nanoantennas. *Nano Lett.* **11,** 2819–2824 (2011).
6. Balistreri, M. L. M., Korterik, J. P., Kuipers, L. & van Hulst, N. F. Local observations of phase singularities in optical fields in waveguide structures. *Phys. Rev. Lett.* **85,** 294–297 (2000).
7. Shalaev, V. M. Optical negative-index metamaterials. *Nature Photon.* **1,** 41–48 (2007).
8. Smith, D. R., Padilla, W. J., Vier, D. C., Nemat-Nasser, S. C. & Schultz, S. Composite medium with simultaneously negative permeability and permittivity. *Phys. Rev. Lett.* **84,** 4184–4187 (2000).
9. Kihm, H. W. *et al.* Bethe-hole polarization analyser for the magnetic vector of light. *Nature Commun.* **2,** 451 (2011).
10. Taminiau, T. H., Karaveli, S., van Hulst, N. F. & Zia, R. Quantifying the magnetic nature of light emission. *Nature Commun.* **3,** 979 (2012).
11. Olmon, R. L. *et al.* Determination of electric-field, magnetic-field, and electric-current distributions of infrared optical antennas: a near-field optical vector network analyzer. *Phys. Rev. Lett.* **105,** 167403 (2010).
12. Devaux, E. *et al.* Local detection of the optical magnetic field in the near zone of dielectric samples. *Phys. Rev. B.* **62,** 10504–10514 (2000).
13. Betzig, E. & Chichester, R. J. Single molecules observed by near-field scanning optical microscopy. *Science* **262,** 1422–1425 (1993).
14. Bozhevolnyi, S. I., Volkov, V. S., Devaux, E., Laluet, J. Y. & Ebbesen, T. W. Channel plasmon subwavelength waveguide components including interferometers and ring resonators. *Nature* **440,** 508–511 (2006).
15. Schnell, M. *et al.* Controlling the near-field oscillations of loaded plasmonic nanoantennas. *Nature Photon.* **3,** 287–291 (2009).
16. Burresi, M. *et al.* Observation of polarization singularities at the nanoscale. *Phys. Rev. Lett.* **102,** 033902 (2009).
17. Kildishev, A. V., Boltasseva, A. & Shalaev, V. M. Planar photonics with metasurfaces. *Science* http://dx.doi.org/10.1126/science.1232009 (2013).
18. Ergin, T., Stenger, N., Brenner, P., Pendry, J. B. & Wegener, M. Three-dimensional invisibility cloak at optical wavelengths. *Science* **328,** 337–339 (2010).
19. Ren, M., Plum, E., Xu, J. & Zheludev, N. I. Giant nonlinear optical activity in a plasmonic metamaterial. *Nature Commun.* **3,** 833 (2012).
20. Soukoulis, M. & Wegener, M. Past achievements and future challenges in the development of three-dimensional photonic metamaterials. *Nature Photon.* **5,** 523–530 (2011).
21. Van Labeke, D. & Barchiesi, D. Probes for scanning tunneling optical microscopy: a theoretical comparison. *J. Opt. Soc. Am. A* **10,** 2193–2201 (1993).
22. Porto, J. A., Carminati, R. & Greffet, J. J. Theory of electromagnetic field imaging and spectroscopy in scanning near-field optical microscopy. *J. Appl. Phys.* **88,** 4845–4850 (2000).
23. Esslinger, M. & Vogelgesang, R. Reciprocity theory of apertureless scanning near-field optical microscopy with point-dipole probes. *ACS Nano* **6,** 8173–8182 (2012).
24. Joannopoulos, J. D., Johnson, S. G., Winn, J. N. & Meade, R. D. in *Photonic Crystals: Molding the Flow of Light* Ch. 7 (Princeton Univ. Press, 2011).
25. Johnson, S. G. & Joannopoulos, J. D. Block-iterative frequency-domain methods for Maxwell's equations in a planewave basis. *Opt. Express* **8,** 173–190 (2001).
26. Engelen, R. J. P., Mori, D., Baba, T. & Kuipers, L. Subwavelength structure of the evanescent field of an optical Bloch wave. *Phys. Rev. Lett.* **102,** 023902 (2009).
27. Kihm, H. W. *et al.* Optical magnetic field mapping using a subwavelength aperture. *Opt. Express* **21,** 5625–5633 (2013).
28. Rotenberg, N. *et al.* Plasmon scattering from single subwavelength holes. *Phys. Rev. Lett.* **108,** 127402 (2012).
29. Yi., J. M. *et al.* Diffraction regimes of single holes. *Phys. Rev. Lett.* **109,** 023901 (2012).
30. Burresi, M. *et al.* Probing the magnetic field of light at optical frequencies. *Science* **326,** 550–553 (2009).

Acknowledgements

The authors thank M. P. van Exter and J. J. Greffet for useful discussions and H. Schoenmaker for fabricating near-field probes. This work is supported by NanoNextNL of the Government of the Netherlands and 130 partners, as well as part of the research programme of the Stichting voor Fundamenteel Onderzoek der Materie (FOM), which is financially supported by the Nederlandse Organisatie voor Wetenschappelijk Onderzoek (NWO). Part of this work was funded by the project 'SPANGL4Q', which has financial support from the Future and Emerging Technologies (FET) programme within the Seventh Framework Programme for Research of the European Commission (FET—Open grant no. FP7-284743).

Author contributions

B.F. and L.K. designed the experiment. B.F. conducted the experiment. N.R. and B.F. analysed the data. D.M.B. fabricated the sample. D.M.B. and B.F. performed simulations. The manuscript was prepared with contributions from all authors.

Additional information

Supplementary information is available in the online version of the paper. Reprints and permissions information is available online at www.nature.com/reprints. Correspondence and requests for materials should be addressed to B.F. and L.K.

Competing financial interests

The authors declare no competing financial interests.